Interface-mediated noble-metal deposition on transition metal dichalcogenide nanostructures

Yifan Sun,[1,2,6] Yuanxi Wang,[2,3,6,7] Jamie Y. C. Chen,[1] Kazunori Fujisawa,[2,3,6] Cameron F. Holder,[1] Jeffery T. Miller,[8] Vincent H. Crespi,[1,2,3,4,6,7,*] Mauricio Terrones,[1,2,3,4,6,*] Raymond E. Schaak[1,2,5,*]

[1]Department of Chemistry, The Pennsylvania State University, University Park, PA, USA. [2]Materials Research Institute, The Pennsylvania State University, University Park, PA, USA. [3]Department of Physics, The Pennsylvania State University, University Park, PA, USA. [4]Department of Materials Science and Engineering, The Pennsylvania State University, University Park, PA, USA. [5]Department of Chemical Engineering, The Pennsylvania State University, University Park, PA, USA. [6]Center for 2-Dimensional and Layered Materials, The Pennsylvania State University, University Park, PA, USA. [7]2-Dimensional Crystal Consortium, The Pennsylvania State University, University Park, PA, USA. [8]Charles D. Davidson School of Chemical Engineering, Purdue University, West Lafayette, IN, USA.

Abstract:

Functionalizing the surfaces of transition metal dichalcogenide (TMD) nanosheets with noble metals is important for electrically contacting them to devices, as well as improving their catalytic and sensing capabilities. Solution-phase deposition provides a scalable approach to creating hybrid metal–TMD systems, but controlling such processes remains challenging. Here, we elucidate the different pathways by which gold and silver deposit at room temperature onto colloidal 1T-WS_2, 2H-WS_2, 2H-$MoSe_2$, 2H-WSe_2, 1T′-$MoTe_2$, and T_d-WTe_2 few-layer nanostructures to produce several distinct classes of 0D–2D and 2D–2D metal–TMD hybrids. Uniform Au nanoparticles form on all TMDs. In contrast, Ag deposits as nanoparticles with a bimodal size distribution on the disulfides and diselenides, and as atomically thin layers on the ditellurides. The various sizes and morphologies of these surface-bound metal species arise from the relative strengths of the interfacial metal–chalcogen bonds during the reduction of Au^{3+} or Ag^{+} by the TMDs.

Layered transition metal dichalcogenides (TMDs) exhibit diverse properties that depend sensitively on their composition, structure, and thickness, and therefore are of significant interest for a broad range of applications.[1–4] TMD heterostructures, which couple together van der Waals solids,[5] molecules,[6] noble metals,[7] quantum dots,[8] layered perovskites,[9] and other materials, further expand the diversity of platforms available for the study of charge transfer, phase transitions, and other short/long range interactions across interfaces. Compared with graphene, which is chemically inert and therefore challenging to functionalize without disturbing the host structure,[10] two-dimensional TMDs are bounded by chalcogen atoms that provide chemical pathways for constructing dimensionally-confined hybrid systems and heterostructures. For example, noble metal atoms and nanoparticles that are covalently bonded to two-dimensional TMD nanosheets yield improved activity and selectivity for various catalytic reactions[11,12] and atomically flat noble metal films are considered a potential pathway toward engineering the electrical contacts required to integrate TMDs into electronic devices.[13,14] The coherent exciton-plasmon coupling within noble metal–TMD heterostructures also induces exotic photonic behavior through nanoscale light-matter interactions.[15,16] Understanding the processes by which nanoscale noble metals deposit on and anchor to TMDs is therefore important for rationally designing novel hybrid functional systems.

Heterostructures consisting of noble metals and TMDs have been prepared by drop-casting solution-dispersed metal nanoparticles on TMD substrates[7,15] and by transferring two-dimensional TMD layers onto patterned noble metal substrates,[17] as well as directly depositing noble metals on TMD nanosheets by electron-beam vapor deposition[18] or solution-based techniques.[11,12] To create heterostructures with the types of precisely tailored interfaces that enable targeted properties and applications, fundamental insights are needed to better understand and control the processes by which hybrids of noble metals and TMDs form and the key structural and electronic characteristics of their interfaces.[19] However, morphologically equivalent TMDs across a wide range of compositions and structures, which are needed to make useful comparisons, have been difficult to produce.

Solution-synthesized colloidal TMD nanosheets offer an advantageous platform for systematically studying noble metal deposition. A library of molybdenum and tungsten disulfides,[20–22] diselenides,[23,24] ditellurides,[25,26] and alloys[26,27] with tunable structures and phases now can be readily synthesized as high surface area nanostructures of the same morphology and size. Additionally, noble metal cations including Au^{3+} and Ag^{+} can be reduced in solution by TMD nanosheets, thus producing metal nanoparticles directly anchored to the TMD surfaces.[12,28] Such processes represent a scalable approach to manufacturing functional heterostructures of noble metals and TMDs, including solution-synthesized colloidal systems that are not confined to substrates and therefore may be applicable to biosensing and catalytic applications.[29,30]

Here, we investigate the room-temperature solution-phase reduction of Au^{3+} and Ag^{+} on colloidal nanostructures comprised of few-layer 1T-WS_2, 2H-WS_2, 2H-$MoSe_2$, 2H-WSe_2, 1T′-$MoTe_2$ and

T_d-WTe_2 nanosheets and elucidate the pathways by which Au and Ag grow on the different TMD substrates. Understanding noble metal deposition across this library of TMD nanostructures, as well as the influence of defects, solvation effects, and interfacial charge transfer on the TMD surfaces, makes it possible to tailor nucleation, growth, structure, and morphology, resulting in a diverse range of 0D–2D nanoparticle–nanosheet and 2D–2D nanosheet–nanosheet hybrid systems. Most notably, strong interactions between silver and tellurium through interfacial Ag–Te bonding and a kinetic preference towards basal plane deposition facilitate the solution-phase deposition of atomically-thin Ag layers on 1T′-$MoTe_2$ and WTe_2. Controllably coupling 0D noble metals and 2D TMDs through interfacial bonds is fundamentally important for designing and constructing new classes of multifunctional heterostructures. For example, solution-phase deposition of atomically-thin noble metal coatings provides a potential synthetic entryway to engineering 2D–2D electrical contacts and substrate-confined single-atom catalysts.

Results and Discussion

Colloidal few-layer nanostructures of 1T-WS_2, 2H-WS_2, 2H-$MoSe_2$, 2H-WSe_2, 1T′-$MoTe_2$, and T_d-WTe_2, which include a range of distinct structures and electronic characteristics, were synthesized using hot-injection reactions at ~300 °C in high boiling organic solvents (Fig. 1a and Supplementary Figs. 1 and 2).[21,25–27] The metal and chalcogen reagents react under these conditions to form two-dimensional nanosheets that grow radially outward from a central core into a flower-like morphology that exposes a high density of surfaces and therefore is ideal for studying the reduction of solvated noble metal cations to nanoparticles on TMD basal planes, as well as the nature of the noble metal/TMD interface. It should be noted that we label nanostructured WS_2 as 1T-WS_2 according to literature precedent for this system,[21] but the experimentally observed structure is 1T′, so 1T′-WS_2 was used for the theoretical calculations (Supplementary Figs. 1 and 6).

Reduction of Au^{3+} on TMD nanostructures. The reduction of Au^{3+} on TMD nanosheets was initiated by injecting a toluene solution containing the colloidally dispersed TMDs into a solution of $HAuCl_4$ in toluene and oleylamine at room temperature. After 10 minutes, the sample was centrifuged, washed, and dried to retrieve the products in powder form. As revealed by the TEM and STEM images shown in Figs. 1b–d and Supplementary Fig. 3, all two-dimensional TMD nanosheets were decorated uniformly with Au nanoparticles. Room-temperature reduction of Au^{3+} to Au^0 typically requires either long aging (up to a few days)[31] or the addition of reducing agents.[32] With the TMD nanosheets present, Au nanoparticles formed within a few minutes at room temperature and without additional reducing agents, suggesting TMDs instead of oleylamine or toluene play the key role in the Au reduction-deposition process.

The Au nanoparticles that grew on the transition metal disulfides and diselenides had average diameters near or less than 3 nm: 1.5 ± 0.3 nm on 1T-WS_2, 1.6 ± 0.3 nm on 2H-WS_2, 1.1 ± 0.2 nm on $MoSe_2$, and 2.9 ± 0.7 nm on WSe_2 (Fig. 1b and Supplementary Fig. 3). In contrast, the Au nanoparticles that grew on the transition metal ditellurides were much larger in diameter: 10.3 ± 2.4 nm on 1T′-$MoTe_2$ and 9.3 ± 2.6 nm on WTe_2 (Fig. 1b and Supplementary Fig. 3). Consistent with the size observations, EDS analysis revealed a significantly larger Au signal relative to the elements present in the TMDs (Mo, W, S, Se, Te) for the ditellurides than for either the disulfides or diselenides (Fig. 1j and Supplementary Fig. 4). Au deposits much more extensively on 1T′-$MoTe_2$ and WTe_2 than on the disulfides and diselenides under otherwise equivalent conditions.

Competition experiments provide further insights into the preferential deposition of Au on transition metal ditellurides. A toluene suspension containing equal amounts of 2H-WS_2 and 1T′-$MoTe_2$ was injected into a solution of $HAuCl_4$ in toluene and oleylamine at room temperature. Figs. 1e–h show a HAADF-STEM image, along with corresponding STEM-EDS element maps, of the product isolated after 10 minutes. In these images, 2H-WS_2 is present in the bottom regions while several 1T′-$MoTe_2$ nanostructures appear throughout. Fig. 1i shows EDS spectra for the regions in Fig. 1e that are labeled “site #1” and “site #2”. At site #1, consisting of Au particles on 1T′-$MoTe_2$, the Au/Mo ratio is 0.74 and large Au particles (~ 10 nm) are visible. At site #2, consisting of Au particles on 2H-WS_2, the Au/W ratio is 0.29 and the particles are too small (< 3 nm) to be seen at this magnification. Both individual and competition experiments were carried out with longer reaction times at room temperature (Supplementary Fig. 5), and as expected, more Au was deposited on the surface of 1T′-$MoTe_2$ relative to 2H-WS_2 from the initial stage (10 min) through saturation (24 h). These experiments for Au deposition on different TMD sheets within the same colloidal environment demonstrate that preferential deposition quickly reaches saturation, which is important for evaluating the electron donating capability of few-layer TMD nanostructures at room temperature.

1T′-$MoTe_2$ and WTe_2, which appear to preferentially deposit Au, are semi-metallic, while the other TMDs are semiconducting. Density functional theory (DFT) calculations were performed to probe how the electronic structures of TMD monolayers allow them to function as electron donors to Au^{3+}. Fig. 2a shows the calculated band alignments of TMDs with respect to the vacuum level. The Fermi energy of monolayer 1T-WS_2 and the vacuum level referenced valence band maximum (negative of ionization potential) of monolayer 2H-WS_2, $MoSe_2$, and WSe_2 are –5.68, –5.75, –5.38 and –5.16 eV, respectively. All of these values are well below the Fermi energies of the ditelluride monolayers, which are –4.44 eV for 1T′-$MoTe_2$ and –4.34 eV for WTe_2. Thus, following the general trend of higher Fermi energies (and band edge energies) and decreasing band gaps (softer Lewis bases) for TMDs with heavier chalcogens, the ditellurides favor electron donation the most, making them best suited for the reduction of Au^{3+} and subsequent Au deposition.[19,33]

The as-synthesized TMD nanosheets contain numerous defects, including metal and chalcogen point vacancies, as well as atomically sharp edges (Supplementary Figs. 6–9). The deposited Au

nanoparticles primarily anchor to edges and step edges on the TMD nanosheets (Fig. 2b and Supplementary Fig. 10), implying defects are the preferred sites where spontaneous reduction of Au^{3+}, and concomitant nucleation and growth of Au nanoparticles, occurs. Defects play a significant role in tuning the electronic structures of two-dimensional TMDs.[34,35] DFT calculations were therefore performed to understand how atomic defects influence the energetics of the Au^{3+} reduction process. As shown in Fig. 2a, Supplementary Fig. 11, and Supplementary Table 1, incorporating ~10% metal or chalcogen atomic vacancies would elevate the valence band maximum of the disulfides and diselenides and thus facilitate the reduction of Au^{3+}. The Fermi levels of the ditellurides are slightly lowered when analogous atomic defects are introduced, but they remain higher than those of the disulfides and diselenides. Therefore, the computational results are consistent with the experimental observation that the amount of reduced Au on the ditellurides significantly exceeds that on the other TMDs, and that the disulfides and diselenides are still able to reduce a limited amount of Au^{3+}, presumably only at highly defective regions.

Reduction of Ag^+ on TMD nanostructures. Distinct from the uniform Au nanoparticles that deposited on the TMD nanostructures, a bimodal distribution of small (2.5 ± 0.4 nm) and large (11.7 ± 2.8 nm) Ag nanoparticles were deposited on transition metal disulfides and diselenides upon reaction with silver acetate at room temperature (Figs. 3a–e, Supplementary Figs. 12 and 13, and Supplementary Table 2). Previous studies of thiol-based self-assembled monolayers on metal surfaces indicated different mobilities and orientations for long-chain thiol molecules on Au vs Ag surfaces, due in part to differences in interfacial metal–sulfur bonding and vacancies.[36,37] Similar factors contribute to the high mobilities of silver ions in silver sulfide ionic conductors.[38,39] It is therefore expected that Ag will have a higher surface mobility than Au, thus leading to greater surface migration and tendency for the smaller Ag clusters to coalesce into larger Ag particles, as has been observed during the growth of Ag on oxide nanoparticle substrates.[40,41] Interestingly, particles were not observed upon reacting the ditellurides (1T′-$MoTe_2$ and WTe_2) with Ag^+ under identical conditions (Figs. 3f and 3g). However, the morphology of the 1T′-$MoTe_2$ and WTe_2 nanostructures was visibly different, with more defined and rounded edges as well as a higher contrast that implies a thicker and/or more electron-dense sample. The structure of the ditelluride nanosheets after Ag^+ reduction, revealed by the ADF-STEM images in Figs. 3f and 3g and the corresponding FFT patterns in the insets, still exhibits the in-plane [002] projections expected for nanosheets of 1T′-$MoTe_2$ and WTe_2, respectively (Supplementary Figs. 14–17); no additional diffraction peaks corresponding to crystalline Ag were observed (Supplementary Fig. 18). In contrast, for the reduction of Au^{3+} on 1T′-$MoTe_2$ and WTe_2, the formation of Au nanoparticles produced diffraction spots corresponding to the expected (111), (200), (220) and (311) planes of Au.

Despite the absence of visible Ag particles, STEM-EDS spectra and element maps both indicate that the ditelluride nanosheets actually contain more Ag than the disulfides or diselenides (Figs. 3h and 3i, and Supplementary Figs. 19 and 20). XRD and Raman data are not consistent with the intercalation of Ag between the TMD layers (Supplementary Fig. 18), suggesting that the Ag is on

the surface of the nanosheets. While ADF-STEM is often used to identify atoms in TMD monolayers, the Z-contrast values are close for Ag and the atoms that comprise the underlying ditelluride substrates, and tilting effects that arise from buckled nanosheets further complicate the analysis that would be necessary to visualize Ag on the TMDs.[27] We therefore prepared and characterized a lower-loading sample containing ~5% of the original amount of Ag [$Ag_{5\%}$/1T′-$MoTe_2$], anticipating that partial deposition of Ag on 1T′-$MoTe_2$ would provide better contrast between regions containing the Ag/1T′-$MoTe_2$ heterostructure and regions of bare 1T′-$MoTe_2$. As shown in Fig. 4a, Ag monolayer regions are observed, and the Ag interfaces epitaxially with the underlying basal plane of 1T′-$MoTe_2$ through Ag (211) planes; the FFT patterns of Ag and 1T′-$MoTe_2$ overlap and thus are difficult to distinguish (Supplementary Figs. 14–17 and 21).[42] A series of ADF-STEM patterns of monolayer and bilayer 1T′-$MoTe_2$, as well as Ag (211) monolayers on monolayer 1T′-$MoTe_2$ with different tilting angles, were also simulated for comparison (Figs. 4b and 4c, and Supplementary Figs. 22 and 23), confirming the formation of the epitaxial Ag/1T′-$MoTe_2$ interface. Additional control experiments varying reaction time, temperature, and solvent (Supplementary Figs. 24–27) further demonstrate the spontaneous formation of 2D Ag coatings with subnanometer thickness, instead of 0D nanoparticles, on the surfaces of 1T′-$MoTe_2$ and WTe_2, indicating that solution-phase deposition can be controlled and dimensionally confined to permit lateral, self-limiting, 2D growth while preventing vertical growth.

Spectroscopic investigation of Ag layers on 1T′-$MoTe_2$ and WTe_2. The formation of Au and Ag nanoparticles on the TMDs can be rationalized by standard processes involving heterogeneous nucleation of seeds followed by homogeneous crystal growth. However, the apparent uniform deposition of atomic Ag layers on transition metal ditellurides (Ag/WTe_2 and Ag/1T′-$MoTe_2$) suggests a fundamentally different formation pathway. X-ray photoelectron spectroscopy (XPS) was used to probe the chemical state of these Ag layers. Fig. 5a shows the Ag Auger spectra and core 3*d* spectra for Ag/WTe_2 and Ag/1T′-$MoTe_2$, as well as Ag_2Te and Ag_2O powders and colloidal Ag nanoparticles (Supplementary Fig. 28) for comparison; the Auger peak is better able than the $3d_{5/2}$ peak to differentiate the Ag oxidation states. Interestingly, the kinetic energies of the Ag M_4VV Auger peaks for Ag/WTe_2 (356.9 eV) and Ag/1T′-$MoTe_2$ (357.1 eV) are closer to the value for Ag_2Te (356.9 eV) than that for Ag nanoparticles (357.8 eV) or Ag_2O (356.0 eV), suggesting an intermediate Ag valence state between Ag^0 and Ag^+ and Ag–Te surface bonding that is similar to Ag_2Te. The Raman features at low wavenumbers (< 150 cm^{-1}) for Ag/WTe_2 and Ag/1T′-$MoTe_2$ also resemble those of Ag_2Te,[43] suggesting that the Ag atoms in the Ag layer are stabilized by bonding to the Te-terminated surface of the ditelluride nanosheets (Supplementary Fig. 29).

Fig. 5a also shows the XPS peaks of the Ag 3*d* electrons for Ag/WTe_2, Ag/1T′-$MoTe_2$, Ag_2Te, Ag_2O, and Ag nanoparticles. The binding energies of the Ag $3d_{5/2}$ peak (referenced to the C1*s* peak at 284.8 eV) for Ag_2O and Ag nanoparticles are indistinguishable at 368.1 eV, while the binding energies of Ag/WTe_2, Ag/1T′-$MoTe_2$, and Ag_2Te are 368.6, 368.6 and 368.4 eV, respectively. The positive chemical shift for Ag/WTe_2, Ag/1T′-$MoTe_2$, and Ag_2Te relative to Ag_2O and Ag

nanoparticles may be caused by lattice potential, extra-atomic relaxation (core-hole screened by atoms other than its host), and/or work function,[44] as well as electronic perturbations from the semi-metallic transition metal ditelluride substrates.[45] Comparing the chemical states of Ag in several Ag-containing materials using an Auger parameter plot (Auger α parameter vs. Ag $3d_{5/2}$ binding energy, shown in Supplementary Fig. 30 and Supplementary Table 3)[46] reveals that Ag/WTe_2, Ag/1T′-$MoTe_2$, and Ag_2Te cluster together while remaining well separated from the other Ag species that include other forms of elemental Ag as well as silver oxides, halides, and chalcogenides.

X-ray absorption spectroscopy (XAS) was used to further study the local environment of the Ag species supported on transition metal ditellurides (Fig. 5b). The Ag K-edge energy (E_o) of Ag/1T′-$MoTe_2$ with the standard Ag loading of 21.8%, Ag/1T′-$MoTe_2$ with a lower Ag loading of ~5% (denoted $Ag_{5\%}$/1T′-$MoTe_2$), and Ag/WTe_2 with the standard Ag loading of 17.7%, as well as bulk Ag_2Te and Ag foil for reference, were determined from the first derivative of the edge. The E_o values for Ag/1T′-$MoTe_2$ (25514.9 eV), $Ag_{5\%}$/1T′-$MoTe_2$ (25515.2 eV), and Ag/WTe_2 (25514.7 eV) are close to that for Ag_2Te (25515.5 eV) and measurably higher than that for Ag foil (25514.0 eV).

The local coordination geometries of Ag/1T′-$MoTe_2$ and Ag/WTe_2 were analyzed by fitting their Fourier-transformed EXAFS spectra using the Ag_2Te structure (Fig. 5c and Supplementary Fig. 31). In contrast to the Ag foil, peaks corresponding to scattering beyond the first coordination sphere were not observed in the spectra of Ag/1T′-$MoTe_2$ and Ag/WTe_2. The magnitude of the most intense peak was also greatly reduced for Ag/1T′-$MoTe_2$ and Ag/WTe_2, where a Ag coordination number around 3 was obtained. The lack of extended bonding and low scattering intensity both support the existence of Ag motifs with very small domains. As shown in Fig. 5c and Supplementary Table 4, first-shell fitting of the highest intensity peak in the Ag/1T′-$MoTe_2$ and Ag/WTe_2 samples resulted in a bond length of 2.80 Å, which is shorter than the Ag–Ag bond (2.89 Å) in bulk Ag and the Ag–Te bonds (2.84–2.91 Å) in bulk Ag_2Te. In 1 nm Pt, Au, and Ag nanoparticles, surface bond lengths are often shorter than in bulk.[47,48] Since 1T′-$MoTe_2$ and WTe_2 layers terminate in Te atoms, we tentatively assign the 2.80 Å scattering to a Ag–Te bond. However, it is challenging to unambiguously identify the atoms giving rise to each individual scattering path given the low-symmetry monoclinic structure of Ag_2Te, which contains multiple Ag–Ag and Ag–Te bonds with similar bonding distances (Supplementary Fig. 31),[49] as well as individual metal–tellurium bonds in 1T′-$MoTe_2$ and WTe_2 that vary slightly in length[50] and that would result in concomitant slight variations in Ag–Te bond lengths. Both types of structural disorder would result in broadened EXAFS peaks and higher $\Delta\sigma^2$ values. For $Ag_{5\%}$/1T′-$MoTe_2$, a similar fitting result with a bond distance of 2.79 Å and a coordination number of 2.9 was obtained, suggesting that the interfacial Ag–Te bonds are maintained for both low and high Ag coverage on the transition metal ditelluride nanostructures.

Together, the microscopic and spectroscopic analyses indicate the formation of atomically thin layers of Ag on the basal planes of 1T′-$MoTe_2$ and WTe_2 through the formation of interfacial Ag–Te bonds. The formation of Ag nanoparticles or thicker Ag layers would exhibit Ag valence states that are closer to metallic Ag and would show evidence of Ag–Ag bonds; neither is observed for Ag/1T′-$MoTe_2$ or Ag/WTe_2. The absence of a plasmon peak further confirms that no Ag nanoparticles are formed (Supplementary Fig. 30).

Computational investigation of Au and Ag on 1T′-$MoTe_2$ and WTe_2. Previously we showed that both Au and Ag reduction on the transition metal ditellurides is thermodynamically favorable (Fig. 2a), using bulk metals as presumed reaction end states. In a first attempt to identify the mechanism for the distinct experimentally observed deposition behaviors of Au and Ag, we now investigated end states alternative to bulk metals, by calculating the formation energies of Au and Ag clusters on 1T′-$MoTe_2$ at different coverages, including single atoms, "stand-up" triangular trimers, and epitaxial thin films interfacing the 1T′-$MoTe_2$ basal plane with the (211) face[51] of bulk Ag or Au (Figs. 6a and 6b). As shown in Figs. 6a and 6b, the formation energies for Ag in these geometries range from +1.3 eV (isolated adsorbed Ag, Ag:Mo = 1:12) to +0.7 eV per metal atom (epitaxial Ag film, Ag:Mo = 3:2) and from +1.8 eV (isolated adsorbed Au, Au:Mo = 1:12) to +0.7 eV for Au (epitaxial Au film, Au:Mo = 3:2). As can be anticipated, formation of metal adsorbates (low-coverage) or films (high-coverage) is not thermodynamically favorable relative to the formation of bulk metal (or near-equivalently, moderate-sized metal nanoparticles). This points to a kinetic argument to rationalize the disparity in the morphologies of reduced Ag vs. Au.

The reduction-deposition process, which begins with solvated metal cations and ends with deposited metal on 1T′-$MoTe_2$, can be summarized in three distinct stages: (1) noble metal salts dissolve in solution and exist as solvated cations, (2) noble metal cations are reduced into neutral atoms adsorbed onto 1T′-$MoTe_2$, and (3) the adsorbed noble metal atoms assemble into bulk metal. The standard reduction potentials, i.e. $E_{red} = E(3) - E(1)$, of Ag^+/Ag^0 and Au^{3+}/Au^0 are both lower than the Fermi levels of the ditellurides, thus the reduction-deposition process is thermodynamically favorable and spontaneous for both Au and Ag. We therefore investigated potentially different kinetic barriers in stage (2), where $E_{barrier} = E(2) - E(1) = E_{red} + E(2) - E(3) \equiv E_{red} + \Delta\mu$, *i.e.* an effective reduction potential that is higher than the standard one by $\Delta\mu$, [52,53] where $\Delta\mu$ is the energy it takes to extract a noble metal atom in its bulk form and let it adsorb onto 1T′-$MoTe_2$. Considering that the products in the two standard reduction half reactions for $Ag^+/Ag(s)$ and $[AuCl_4]^-/Au(s)$ are bulk metals with reduction potentials of –5.24 eV and –5.44 eV relative to vacuum (or 0.80 V and 1.00 V relative to SHE), the calculated $\Delta\mu$ for Ag and Au adsorbed on 1T′-$MoTe_2$ are $\Delta\mu_{Ag/1T'\text{-}MoTe2} = \mu_{Ag/1T'\text{-}MoTe2} - \mu_{Ag,bulk} = 1.33$ eV and $\Delta\mu_{Au/1T'\text{-}MoTe2} = \mu_{Au/1T'\text{-}MoTe2} - \mu_{Au,bulk} = 1.80$ eV, respectively, where $\mu_{metal,adsorbed} = E_{metal/1T'\text{-}MoTe2} - E_{1T'\text{-}MoTe2}$ and $\mu_{metal,bulk}$ is the per-atom energy of the bulk metal. Thus, as shown in Fig. 6c, the effective reduction potentials for the adsorbed Ag and Au atoms on 1T′-$MoTe_2$ become –5.24 + 1.33 = –3.91 eV (relative to vacuum) and –5.44 + 1.80 = –3.64 eV (relative to vacuum), respectively. A similar disparity between the relative stabilities of isolated atoms for Ag and Au is found for adsorption

on WTe_2 ($\Delta\mu_{Ag/WTe2}$ = 1.31 eV, $\Delta\mu_{Au/WTe2}$ = 1.76 eV), which yields differences in nucleation barriers similar to the case of 1T′-$MoTe_2$.

Solvation effects are also taken into consideration for the adsorbed gold and silver atoms on 1T′-$MoTe_2$. Calculations using two different solvation models (see Supplementary Information for details) yielded the same result: the solvation energies of Ag/1T′-$MoTe_2$ and Au/1T′-$MoTe_2$ are 0.12 eV and <0.01 eV, respectively. Thus taking the Fermi level of 1T′-$MoTe_2$ to be –4.44 eV, the kinetic barriers to forming an adsorbed Ag and Au atom are $\Delta\mu_{Ag/1T'\text{-}MoTe2}$ = 4.44 – 3.91 – 0.12 = 0.41 eV for Ag/1T′-$MoTe_2$ and $\Delta\mu_{Au/1T'\text{-}MoTe2}$ = 4.44 – 3.64 = 0.80 eV for Au/1T′-$MoTe_2$ (Fig. 6c). Since the initial concentrations of Ag^+ and Au^{3+} are the same, the reaction rates are determined by reaction barriers, with the rates of atomic Ag deposition being faster than those of atomic Au deposition by an estimated $e^{-0.41/0.026}$ / $e^{-0.80/0.026} \approx 3\times10^6$ at room temperature. Thus a difference in the kinetic barriers for Au and Ag during nucleation may lead to Ag preferentially forming 2D atomic layers on 1T′-$MoTe_2$ and Au adsorbing only onto existing Au and forming 0D nanoparticles (Supplementary Fig. 32). Additional hybrid functional calculations suggesting even lower barriers for adsorbed Ag are detailed in the Supplementary Information.

The larger solvation energy for Ag adsorbed on the transition metal ditellurides originates from its larger degree of ionicity as an adsorbate, as analyzed using electron transfer magnitudes from DFT calculations. Real-space charge differences [*xy*-integrated into $\Delta\rho(z)$ and further integrated along the out-of-plane direction from vacuum to the zero-crossing point of $\Delta\rho(z)$] indicate that the charge transfer from an adsorbed Ag atom to 1T′-$MoTe_2$, ~0.116 electrons, is much larger than that from an adsorbed Au atom, ~0.006 electrons, as shown in Fig. 6d. These are qualitatively consistent results from the projected band structure analysis shown in Supplementary Fig. 33 and quantitatively consistent with the overall vertical dipole moment of +0.38 and +0.02 e·Å calculated for Ag/1T′-$MoTe_2$ and Au/1T′-$MoTe_2$, respectively, if a charge separation of ~3 Å is used (see Supplementary Information for further details on Bader analysis). This suggests that adsorption onto 1T′-$MoTe_2$ increases the oxidation state of Ag due to electron donation, as reflected in the XPS spectra (Supplementary Fig. 34 and Supplementary Tables 3 and 5). It is possible that this difference in the degree of charge transfer between Ag/1T′-$MoTe_2$ and Au/1T′-$MoTe_2$ not only facilitates Ag adsorption onto 1T′-$MoTe_2$ by stabilizing the Ag/1T′-$MoTe_2$ structure through electrostatic screening from the solvent, but also prevents Ag^+ cations from approaching an existing adsorbed Ag atom, being reduced, and adsorbing onto existing Ag to form nanoparticles, since both Ag species are positively charged.

Conclusions

Solution-phase reduction-deposition of Au and Ag on colloidal transition metal disulfides, diselenides, and ditellurides proceeds through different pathways and results in distinct classes of 0D–2D and 2D–2D metal/TMD hybrids. The ditellurides (1T′-$MoTe_2$ and WTe_2) exhibit stronger reducing capabilities relative to the disulfides (1T-WS_2 and 2H-WS_2) and diselenides ($MoSe_2$ and

WSe_2) during the spontaneous reduction process, which is attributed to the higher Fermi levels and semi-metallic nature. Upon reduction, the as-reduced Au and Ag atoms stack in different arrangements, mediated by the noble metal/TMD interface. Uniform Au nanoparticles form on all TMDs, while a bimodal distribution of Ag nanoparticles forms on disulfides and diselenides, which can be correlated with the relative strengths of the interfacial noble metal–chalcogen bonds. Most notably, Ag deposits on 1T′-$MoTe_2$ and WTe_2 as atomically-thin layers stabilized by interfacial Ag–Te bonds, a distinct behavior that we attribute to a lower kinetic barrier for Ag compared to Au at the initial nucleation stage. These fundamental insights into the solution-phase deposition of Au and Ag onto colloidal TMD nanosheets are important for emerging and future applications of TMDs and metal–TMD heterostructures. For example, the ability to access atomically-thin Ag layers on 1T′-$MoTe_2$ and WTe_2, and understanding how such unique nanostructures form, will be important for designing and synthesizing single-atom catalysts, where chemisorption and chemoselectivity could be modified via electronic interactions.[54] The formation of unique 2D atomic architectures of noble metals supported on TMD nanostructures also provides a potential route to increase catalyst loading without aggregation, and therefore retaining active species that are based on atomic-level constructs. In addition, atomic-level engineering of electrical contacts between TMDs and noble metals could be approached through solution-phase deposition, where chemical disorder and Fermi-level pinning at the noble metal/TMD interface are effectively mitigated.[55]

Methods

Materials. Oleylamine (technical grade, 70%), hexamethyldisilazane (HMDS, reagent grade, ⩾ 99%), carbon disulfide (CS_2, ⩾ 99.9%, anhydrous), tungsten (VI) chloride (WCl_6, ⩾ 99.9%, trace metals basis), gold (III) chloride trihydrate ($HAuCl_4 \cdot 3H_2O$, ⩾ 99.9%, trace metals basis), gold (I) chloride (AuCl, 99.9%, trace metals basis), silver (I) sulfide (Ag_2S, 99.99%, trace metals basis), silver (I) selenide (Ag_2Se), and silver (I) telluride (Ag_2Te) were purchased from Sigma Aldrich. Oleic acid (technical grade, 90%), molybdenum(V) chloride ($MoCl_5$, 99.6%, metals basis), selenium powder (-325 mesh, 99.5%, metals basis), tellurium powder (-200 mesh, 99.5%, metal basis), and silver (I) acetate (CH_3COOAg, anhydrous, 99%) were purchased from Alfa Aesar. Tri-n-octylphosphine (TOP, ⩾85%) was purchased from TCI America. Solvents, including toluene and ethanol, were of analytical grade. All chemicals were used as received without further purification.

Synthesis of TMD nanostructures. All reactions were carried out under an argon atmosphere using standard Schlenk techniques and workup procedures were performed in air. The 1T-WS_2, 2H-WS_2, 2H-$MoSe_2$, 2H-WSe_2, 1T′-$MoTe_2$, and T_d-WTe_2 nanostructures were synthesized according to previous reports.[21,25–27] The as-obtained TMD samples were stored as powders under argon to minimize surface oxidation.

Noble metal deposition on TMD nanostructures. Noble metal reagents (0.2 mmol, 78.8 mg $HAuCl_4 \cdot 3H_2O$, or 33.4 mg CH_3COOAg) were dissolved in a mixture of oleylamine (5 mL, 15.2 mmol) and toluene (5 mL, 47.0 mmol) and then transferred to a 100-mL three-neck flask under a flow of argon. Meanwhile, 0.015 mmol of the nanostructured TMD samples were dispersed in 1 mL of toluene (9.4 mmol) and rapidly injected at room temperature (25 °C) into the solution containing noble metal reagents. After 10 min, the reaction was stopped by centrifuging and collecting the products, which were then washed with a 1:1 toluene/ethanol mixture and kept as powders under argon for characterization. For lower loadings of Ag, all of the operations remained the same except decreasing the amount of the noble metal reagent from 0.2 mmol to 0.01 mmol. Colloidal Ag nanoparticles for XPS characterization were prepared by dissolving 100 mg of silver acetate (0.6 mmol) in a mixture of oleylamine (10 mL, 30.4 mmol) and toluene (10 mL, 94.1 mmol) and heating under argon at 100 °C for 1 h. Colloidal Au nanoparticles were prepared according to a previous report.[32]

Characterization. Powder XRD patterns were collected using a Bruker-AXS D8 Advance diffractometer equipped with Cu Kα radiation and a LynxEye 1-D detector. TEM, HAADF-STEM images, and EDS data with element maps were acquired using a FEI Talos F200X operating at 200 kV. High-resolution ADF images were obtained using a FEI Titan^3 G2 60/300 TEM with a spherical aberration corrector on both the probe-and the image-forming lens at an accelerating voltage of 80 kV. ADF-STEM image simulation was done by QSTEM software developed by C. Koch.[56] All parameters for the ADF image simulation were appropriately set according to experimental imaging conditions, including acceleration voltage, spherical aberration (C_3 and C_5), convergence angle, and inner/outer angle for the ADF detector. Thermal diffuse scattering (TDS) was taken into account and tilting angle was applied by QSTEM software by rotating the sample structure. The FFT patterns were obtained from replicated simulated ADF-STEM images. Bruker ESPRIT 2 software was applied for EDS data interpretation. Micro-Raman measurements were performed in a Renishaw inVia confocal microscope-based Raman spectrometer with 514.5 nm laser. XPS experiments were performed using a Physical Electronics VersaProbe II instrument equipped with a monochromatic Al Kα X-ray source (hν = 1486.7 eV) and a concentric hemispherical analyzer. Peaks were charge referenced to the CH_x peak in the carbon 1s spectra at 284.8 eV. Measurements were made at a takeoff angle of 45° with respect to the sample surface plane, which resulted in a typical sampling depth of 3-6 nm. Quantification was carried out using instrumental relative sensitivity factors (RSFs) that account for the X-ray cross section and inelastic mean free path of the electrons. The Auger spectra possess a two-hole final state, thus providing valuable information about the electronic states of the target element without being affected by switching excitation lasers or applying various charging correction standards when plotted against kinetic energy. Ag K-edge (25.514 keV) X-ray absorption measurements were conducted on the bending magnet beamline of the Materials Research Collaborative Access Team (MRCAT 10-BM) at the Advanced Photon Source (APS) at Argonne National Laboratory. More details over sample preparation and data collection are included in the Supplementary Information.

XAS spectra were analyzed using WinXAS 3.1 software and normalized with linear and cubic fits of the pre-edge and post-edge regions, respectively. Fitting of the Ag coordination sphere were obtained by fitting the Fourier transform of the k^2-weighted EXAFS from k = 2.5–10.5 $Å^{-1}$ and R = 2.15–3.2 Å using Ag_2Te scattering path calculated using FEFF 9.0.[49,57]

Theoretical Calculations. For Ag/1T′-$MoTe_2$, formation energies are given by $E_{form} = (E_{Ag\times n/1T'\text{-}MoTe2} - E_{1T'\text{-}MoTe2})/n - E_{Ag(bulk)}$, where n is the number of metal atoms in the calculation cell and where we approximate the energy per metal atom in a fully grown nanoparticle to be that of the bulk metal $E_{Ag(bulk)}$ (accurate within ~0.1 eV for nanoparticles larger than 1.5 nm). Thermodynamic comparisons using first-principles calculations require accurate descriptions of silver and gold in both their bulk and atomic forms. While the capability of Kohn-Sham DFT within the generalized gradient approximation to describe atomization energies is limited,[58] for the subset of common noble metals (e.g. Au, Ag, Pt) the PBE functional with DFT-D3 van der Waals corrections by Grimme (hereafter PBE-D3) outperforms other commonly benchmarked functionals, including meta-GGA functionals (TPSS) and hybrid functionals (PBE0),[59] with cohesive energies at 2.98 and 3.76 eV for bulk silver and gold, compared with 2.95 and 3.81 eV from experiments.[60] The employment of scalar relativistic pseudopotentials (included in the above energies) has only negligible effects on the cohesive energy of silver (10 meV difference) but was crucial for the case of gold (130 meV difference). Adsorption energies between silver atoms and layered solids (e.g. graphene) from our test calculations using PBE-D3 also agrees well with that calculated from coupled-cluster theory.[61] Thus the choice of PBE-D3 ensures an overall consistent usage of exchange-correlation functional across all calculated species while maintaining accuracy. The reduction potentials estimated here are based on standard aqueous conditions; similar estimates for non-aqueous solutions (toluene in our case) are more challenging and are discussed in the Supplementary Information, together with additional details on the implementation of first-principles calculations.

To accurately account for the effects of defects on band edges, we followed the following procedure. 10 samples of 6×6 TMD supercells were generated with randomized defect positions for each type of defect and each type of TMD separately, with appropriate defect concentrations [a total of 10 samples × 6 TMDs × (2 levels of concentrations for chalcogen vacancy + 1 level of concentration for metal vacancy) = 180 structures]. We considered chalcogen vacancy with concentrations of 5.6 and 12.5 at.% (4 and 9 defects per supercell, respectively) and metal vacancy with concentrations of 11.1 at.% (4 random defects per supercell). The highest valence band maximum for each set of 10 structures is taken as the valence band maxima for that case.

Reference

1. Wang, Q. H., Kalantar-Zadeh, K., Kis, A., Coleman, J. N. & Strano, M. S. Electronics and optoelectronics of two-dimensional transition metal dichalcogenides. *Nat. Nanotechnol.* **7**, 699–712 (2012).

2. Lv, R. *et al.* Transition metal dichalcogenides and beyond: synthesis, properties, and applications of single- and few-layer nanosheets. *Acc. Chem. Res.* **48**, 56–64 (2015).

3. Jaramillo, T. F. *et al.* Identification of active edge sites for electrochemical H_2 evolution from MoS_2 nanocatalysts. *Science* **317**, 100–102 (2007).

4. Ali, M. N. *et al.* Large, Non-saturating magnetoresistance in WTe_2. *Nature* **514**, 205–208 (2014).

5. Gong, Y. *et al.* Vertical and in-plane heterostructures from WS_2/MoS_2 monolayers. *Nat. Mater.* **13**, 1135–1142 (2014).

6. Voiry, D. *et al.* Covalent functionalization of monolayered transition metal dichalcogenides by phase engineering. *Nat. Chem.* **7**, 45–49 (2014).

7. Kang, Y. *et al.* Plasmonic hot electron induced structural phase transition in a MoS_2 monolayer. *Adv. Mater.* **26**, 6467–6471 (2014).

8. Chen, J. *et al.* Edge epitaxy of two-dimensional $MoSe_2$ and MoS_2 nanosheets on one-dimensional nanowires. *J. Am. Chem. Soc.* **139**, 8653–8660 (2017).

9. Kang, D.-H. *et al.* An ultrahigh-performance photodetector based on a perovskite-transition-metal-dichalcogenide hybrid structure. *Adv. Mater.* **28**, 7799–7806 (2016).

10. Chhowalla, M. *et al.* The chemistry of two-dimensional layered transition metal dichalcogenide nanosheets. *Nat. Chem.* **5**, 263–275 (2013).

11. Li, H. *et al.* Synergetic interaction between neighbouring platinum monomers in CO_2 hydrogenation. *Nat. Nanotechnol.* **13**, 411–417 (2018).

12. Huang, X. *et al.* Solution-phase epitaxial growth of noble metal nanostructures on dispersible single-layer molybdenum disulfide nanosheets. *Nat. Commun.* **4**, 1444 (2013).

13. Liu, Y. *et al.* Approaching the Schottky-Mott limit in van der Waals metal-semiconductor junctions. *Nature* **557**, 696–700 (2018).

14. Popov, I., Seifert, G. & Tománek, D. Designing electrical contacts to MoS_2 monolayers: a computational study. *Phys. Rev. Lett.* **108**, 156802 (2012).

15. Zhao, W. *et al.* Exciton-plasmon coupling and electromagnetically induced transparency in monolayer semiconductors hybridized with Ag nanoparticles. *Adv. Mater.* **28**, 2709–2715 (2016).

16. Zheng, D. *et al.* Manipulating coherent plasmon–exciton interaction in a single silver nanorod on monolayer WSe_2. *Nano Lett.* **17**, 3809–3814 (2017).

17. Najmaei, S. *et al.* Plasmonic pumping of excitonic photoluminescence in hybrid MoS_2-Au nanostructures. *ACS Nano* **8**, 12682–12689 (2014).

18. Gong, C. *et al.* Metal contacts on physical vapor deposited monolayer MoS_2. *ACS Nano* **7**, 11350–11357 (2013).

19. Lei, S. *et al.* Surface functionalization of two-dimensional metal chalcogenides by Lewis acid–base chemistry. *Nat. Nanotechnol.* **11**, 465–471 (2016).

20. Son, D. *et al.* Colloidal synthesis of uniform-sized molybdenum disulfide nanosheets for wafer-scale flexible nonvolatile memory. *Adv. Mater.* **28**, 9326–9332 (2016).

21. Mahler, B., Hoepfner, V., Liao, K. & Ozin, G. A. Colloidal synthesis of 1T-WS_2 and 2H-WS_2 nanosheets: applications for photocatalytic hydrogen evolution. *J. Am. Chem. Soc.* **136**, 14121–14127 (2014).

22. Yoo, D., Kim, M., Jeong, S., Han, J. & Cheon, J. Chemical synthetic strategy for single-layer transition-metal chalcogenides. *J. Am. Chem. Soc.* **136**, 14670–14673 (2014).

23. Jung, W. *et al.* Colloidal synthesis of single-Layer MSe_2 (M = Mo, W) nanosheets via anisotropic solution-phase growth approach. *J. Am. Chem. Soc.* **137**, 7266–7269 (2015).

24. Sun, D., Feng, S., Terrones, M. & Schaak, R. E. Formation and interlayer decoupling of colloidal $MoSe_2$ nanoflowers. *Chem. Mater.* **27**, 3167–3175 (2015).

25. Sun, Y. *et al.* Low-temperature solution synthesis of few-layer 1T′-$MoTe_2$ nanostructures exhibiting lattice compression. *Angew. Chem. Int. Ed.* **55**, 2830–2834 (2016).

26. Sun, Y., Fujisawa, K., Terrones, M. & Schaak, R. E. Solution synthesis of few-layer WTe_2 and $Mo_xW_{1-x}Te_2$ nanostructures. *J. Mater. Chem. C* **5**, 11317–11323 (2017).

27. Sun, Y. *et al.* Low-temperature solution synthesis of transition metal dichalcogenide alloys with tunable optical properties. *J. Am. Chem. Soc.* **139**, 11096–11105 (2017).

28. Kim, J., Byun, S., Smith, A. J., Yu, J. & Huang, J. Enhanced electrocatalytic properties of transition-metal dichalcogenides sheets by spontaneous gold nanoparticle decoration. *J. Phys. Chem. Lett.* **4**, 1227–1232 (2013).

29. Yeh, Y.-T. *et al.* Light-emitting transition metal dichalcogenide monolayers under cellular digestion. *Adv. Mater.* **30**, 1703321 (2018).

30. Raza, F. *et al.* Structuring Pd nanoparticles on 2H-WS_2 nanosheets induces excellent photocatalytic activity for cross-coupling reactions under visible light. *J. Am. Chem. Soc.* **139**, 14767–14774 (2017).

31. Huo, Z., Tsung, C., Huang, W., Zhang, X. & Yang, P. Sub-two nanometer single crystal Au nanowires. *Nano Lett.* **8**, 2041–2044 (2008).

32. Peng, S. *et al.* A facile synthesis of monodisperse Au nanoparticles and their catalysis of CO oxidation. *Nano Res.* **1**, 229–234 (2008).

33. Choi, H. C., Shim, M., Bangsaruntip, S. & Dai, H. Spontaneous reduction of metal ions on the sidewalls of carbon nanotubes. *J. Am. Chem. Soc.* **124**, 9058–9059 (2002).

34. Zhou, W. *et al.* Intrinsic structural defects in monolayer molybdenum disulfide. *Nano Lett.* **13**, 2615–2622 (2013).

35. Sun, Y. *et al.* Defect-mediated selective hydrogenation of nitroarenes on nanostructured WS_2. *Chem. Sci.* **10**, 10310–10317 (2019).

36. Ulman, A. Formation and structure of self-assembled monolayers. *Chem. Rev.* **96**, 1533–1554 (1996).

37. Laibinis, P. E. *et al.* Comparison of the structures and wetting properties of self-assembled monolayers of n-alkanethiols on the coinage metal surfaces, copper, silver, and gold. *J. Am. Chem. Soc.* **113**, 7152–7167 (1991).

38. Hebb, M. H. Electrical conductivity of silver sulfide. *J. Chem. Phys.* **20**, 185–190 (1952).

39. Elliott, S. R. A unified mechanism for metal photodissolution in amorphous chalcogenide materials. *J. Non-Cryst. Solids* **130**, 85–97 (1991).

40. Hodges, J. M., Morse, J. R., Williams, M. E. & Schaak, R. E. Microscopic investigation of chemoselectivity in Ag-Pt-Fe_3O_4 heterotrimer formation: mechanistic insights and implications for controlling high-order hybrid nanoparticle morphology. *J. Am. Chem. Soc.* **137**, 15493–15500 (2015).

41. Ridelman, Y. *et al.* Metallic nanobowls by galvanic replacement reaction on heterodimeric nanoparticles. *Small* **8**, 654–660 (2012).

42. Hla, S. W., Prodan A. & van Midden H. J. P. Atomistic stress fluctuation at surfaces and edges of epitaxially grown silver nanorods. *Nano Lett.* **4**, 1221–1224 (2004).

43. Milenov, T. I. *et al.* Preliminary studies of the Raman spectra of Ag_2Te and Ag_5Te_3. *Opt. Quant. Electron.* **46**, 573–580 (2014).

44. Gaarenstroom, S. W. & Winograd, N. Initial and final state effects in the ESCA spectra of cadmium and silver oxides. *J. Chem. Phys.* **67**, 3500–3506 (1977).

45. Rodriguez, J. A. & Goodman, D. W. Surface science studies of the electronic and chemical properties of bimetallic systems. *J. Phys. Chem.* **95**, 4196–4206 (1991).

46. Hu, P. *et al.* Electronic metal-support interactions in single-atom catalysts. *Angew. Chem. Int. Ed.* **53**, 3418–3421 (2014).

47. Miller, J. T. *et al.* The effect of gold particle size on the Au-Au bond distance and ractivity toward oxygen in supported catalysts. *J. Catal.* **240**, 222–234 (2006).

48. Wei, H. *et al.* Selective hydrogenation of acrolein on supported silver catalysts: A kinetic study of particle size effects. *J. Catal.* **298**, 18–26 (2013).

49. van der Lee, A. & de Boer, J. L. Redetermination of the structure of hessite, Ag_2Te-III. *Acta Cryst. C* **49**, 1444–1446 (1993).

50. Dawson, W. & Bullett, D. Electronic structure and crystallography of $MoTe_2$ and WTe_2. *J. Phys. C* **20**, 6159–6174 (1987).

51. Hla, S. W., Marinković, V. & Prodan, A. The growth of gold on (001) surfaces of α- and β-$MoTe_2$. *Surf. Sci.* **356**, 130–136 (1996).

52. Plieth, W. J. Electrochemical properties of small clusters of metal atoms and their role in the surface enhanced Raman scattering. *J. Phys. Chem.* **86**, 3166–3170 (1982).

53. Tang, L. *et al.* Electrochemical stability of nanometer-scale Pt particles in acidic environments. *J. Am. Chem. Soc.* **132**, 596–600 (2010).

54. Tauster, S. J., Fung, S. C., Baker, R. T. K. & Horsley, J. A. Strong interactions in supported-

metal catalysts. *Science* **211**, 1121–1125 (1981).

55. Wang, Y. *et al.* Van der Waals contacts between three-dimensional metals and two-dimensional semiconductors. *Nature* **568**, 70–74 (2019).

56. Koch, C. T. Determination of core structure periodicity and point defect density along dislocations. PhD Thesis, Arizona State University (2002).

57. Rehr, J. J., Kas, J. J., Vila, F. D., Prange, M. P. & Jorissen, K. Parameter-free calculations of X-ray spectra with FEFF9. *Phys. Chem. Chem. Phys.* **12**, 5503 (2010).

58. Perdew, J. P. *et al.* Restoring the density-gradient expansion for exchange in solids and surfaces. *Phys. Rev. Lett.* **100**, 136406 (2008).

59. Tran, F., Stelzl, J. & Blaha, P. Rungs 1 to 4 of DFT Jacob's ladder: Extensive test on the lattice constant, bulk modulus, and cohesive energy of solids. *J. Chem. Phys.* **144**, 204120 (2016).

60. Elsasser, C. *et al.* Relativistic effects on ground state properties of 4d and 5d transition metals. *J. Phys. Condens. Matter* **2**, 4371–4394 (1990).

61. Granatier, J., Lazar, P., Otyepka, M. & Hobza, P. The nature of the binding of Au, Ag, and Pd to benzene, coronene, and graphene: From benchmark CCSD(T) calculations to plane-wave DFT calculations. *J. Chem. Theory Comput.* **7**, 3743–3755 (2011).

Acknowledgements

Y.S. and R.E.S. were supported by the U.S. National Science Foundation Grant DMR-1607135 for the initial synthesis of the TMD nanostructures and CHE-1707830 for the studies involving deposition of Au and Ag. Y.W. and V.H.C. acknowledge the National Science Foundation Materials Innovation Platform Two-Dimensional Crystal Consortium under DMR-1539916. J.Y.C.C. and C.F.H. were supported by funds from Penn State University. Y.S., K.F. and M.T. acknowledge support from the Air Force Office of Scientific Research (AFOSR) grant 17RT0244. J.T.M. was supported by the National Science Foundation under Cooperative Agreement No. EEC-1647722. V.H.C. and M.T. also acknowledge the Center for 2-Dimensional and Layered Materials at the Pennsylvania State University. Electron microscopy and XPS were performed at the Electron Microscopy Facility at the Materials Characterization Lab of the Penn State Materials Research Institute. Use of the Advanced Photon Source (APS) is supported by the U.S. Department of Energy, Office of Science, and Office of Basic Energy Sciences, under Contract DE-AC02-06CH11357. MRCAT operations, beamline 10-BM, are supported by the Department of Energy and the MRCAT member institutions. We thank John Katsoudas and Joshua Wright for the assistance during XAS experiments at the 10-BM beamline at the APS at Argonne National Laboratory. We also thank Jennifer Grey and Ke Wang for assistance with TEM characterization and Jeff Shallenberger for XPS acquisition and analysis.

Author contributions

Y.S. carried out all the synthetic work and characterization by XRD, TEM, HAADF-STEM, STEM-EDS and Raman. Y.W. and V.H.C. performed the DFT calculations. J.Y.C.C., C.F.H., and Y.S. conducted the XAS measurements. J.Y.C.C. and J.T.M. analyzed EXAFS and XANES data. C.F.H. also carried out XPS acquisition and analysis for part of the samples. K.F. carried out the high-resolution ADF-STEM imaging and simulation. M.T. and R.E.S. conceived and directed the project. Y.S., Y.W., J.Y.C.C., V.H.C., M.T., and R.E.S. prepared the manuscript.

Additional information

The authors declare no competing interests.

Data availability

The data that support the findings of this study are available from the corresponding authors upon reasonable request.

Figure Captions

Fig. 1 | Reduction of Au^{3+} on TMD nanostructures. a, TEM images of each type of TMD nanostructure: 1T-WS_2, 2H-WS_2, $MoSe_2$, WSe_2, 1T′-$MoTe_2$, and WTe_2. **b**, TEM images of each type of TMD nanostructure after reaction with Au^{3+}, which produces Au nanoparticles anchored to the TMD nanosheet surfaces. Drawings below the TEM images, which include few-layer TMD nanosheets and anchored Au particles, highlight the key features of each system. **c**,**d**, HAADF-STEM images of Au/1T-WS_2 (**c**) and Au/1T′-$MoTe_2$ (**d**). **e**, HAADF-STEM image showing the product of the competitive deposition of Au^{3+} on a physical mixture of 1T′-$MoTe_2$ and 2H-WS_2. **f**–**h**, EDS elemental maps for Mo (**f**) and W (**g**), as well as a schematic showing the preferential deposition of Au on 1T′-$MoTe_2$ relative to 2H-WS_2 (**h**), are also shown. **i**, EDS spectra for site #1 (Au/1T′-$MoTe_2$) and site #2 (Au/2H-WS_2), as identified in Fig. 1e by green and blue boxes, respectively. **j**, Plot showing the percentage of Au from EDS analysis (Supplementary Fig. 4), associated with the left-hand axis, and Au nanoparticle size from TEM and STEM images, associated with the right-hand axis, for each Au/TMD nanostructure. At least 50 nanoparticles were analyzed for the size-distribution measurement and error bars were determined by averaging data from five distinct samples.

Fig. 2 | Influence of electronic structure and structural defects on the reduction of Au^{3+} on TMD nanostructures. a, Band alignment diagram for monolayer (dark green) and bulk (light green) 1T-WS_2, 2H-WS_2, 2H-$MoSe_2$, 2H-WSe_2, 1T′-$MoTe_2$ and T_d-WTe_2, as well as Au^{3+}/Au^0 and Ag^+/Ag^0 reduction potentials drawn as orange and grey lines, respectively. Vertical bars span the band gaps. For metals, the band gaps collapse into lines, which indicate the Fermi levels. The blue dotted lines indicate the range of the Fermi level changes caused by incorporation of 12.5% chalcogen or 11.1% metal atomic vacancies, as shown in Supplementary Table 1. **b**, Atomic-resolution ADF-STEM images of Au/WTe_2 from basal plane and cross-section views (inset), where most Au nanoparticles are situated on the edges and step edges of the WTe_2 nanosheets.

Fig. 3 | Reduction of Ag^+ on TMD nanostructures. a, Drawing depicting the bimodal distribution of Ag nanoparticles deposited on transition metal disulfide and diselenide nanostructures. **b**–**e**, HAADF-STEM image of Ag/1T-WS_2 (**b**) and TEM images of Ag/2H-WS_2 (**c**), Ag/$MoSe_2$ (**d**), and Ag/WSe_2 (**e**). **f**, Reduction of Ag^+ on transition metal ditelluride nanostructures: TEM images before (i) and after the reduction of Ag^+ on 1T′-$MoTe_2$ (ii); High-magnification ADF-STEM image of Ag/1T′-$MoTe_2$ (iii) with corresponding FFT pattern in the inset. **g**, TEM images before (i) and after the reduction of Ag^+ on WTe_2 (ii); High-magnification ADF-STEM image of Ag/WTe_2 (iii) with corresponding FFT pattern in the inset. **h**, EDS spectra corresponding to the Ag/1T′-$MoTe_2$ and Ag/WTe_2 samples, confirming the presence of Ag deposited on the ditelluride nanostructures.

i, Plot showing the percentage of Ag from EDS analysis (Fig. 3h and Supplementary Fig. 19), associated with the left-hand axis, and Ag nanoparticle size from TEM and STEM images, associated with the right-hand axis, for each Ag/TMD nanostructures. At least 50 nanoparticles were analyzed for the size-distribution measurement and error bars were determined by averaging data from five distinct samples.

Fig. 4 | Microscopic evidence of atomic Ag layers deposited on the 1T′-$MoTe_2$ nanostructures. **a**, Atomic-resolution ADF-STEM image of $Ag_{5\%}$/1T′-$MoTe_2$. Ag (211) planes deposited epitaxially on monolayer 1T′-$MoTe_2$ and bilayer 1T′-$MoTe_2$ are highlighted with dashed orange and black boxes, respectively. The corresponding simulated ADF-STEM patterns are shown inside the adjacent solid boxes for comparison. **b**, Simulated ADF-STEM images of the basal plane of monolayer 1T′-$MoTe_2$ (i) and bilayer 1T′-$MoTe_2$ (ii), as well as Ag (211) monolayer epitaxially deposited on monolayer 1T′-$MoTe_2$ (iii), with the electron beam perpendicular to the plane. **c**, Simulated ADF-STEM images of the basal plane of monolayer 1T′-$MoTe_2$ (i) and bilayer 1T′-$MoTe_2$ (ii), as well as Ag (211) monolayer epitaxially deposited on monolayer 1T′-$MoTe_2$ (iii), with the electron beam parallel to the *c* axis of 1T′-$MoTe_2$ (3.96° tilt angle relative to the 1T′-$MoTe_2$ basal plane).

Fig. 5 | Spectroscopic investigation of Ag/1T′-$MoTe_2$ and Ag/WTe_2. **a**, Ag Auger (left) and 3*d* XPS spectra (right) of bulk powders of Ag_2O and Ag_2Te reference samples, Ag/1T′-$MoTe_2$ and Ag/WTe_2 via reduction of Ag^+ on the 1T′-$MoTe_2$ and WTe_2 nanostructures, and colloidal Ag nanoparticles (NPs). A TEM image of the colloidal Ag nanoparticles is shown in Supplementary Fig. 28. All spectra were calibrated with the C1*s* peak at 284.8 eV. **b**,**c**, Ag-K edge XAS spectra (**b**) and corresponding k^2-weighted Fourier transform spectra (**c**) of Ag foil, Ag/WTe_2, Ag/1T′-$MoTe_2$, $Ag_{5\%}$/1T′-$MoTe_2$, and Ag_2Te bulk powders. For Ag/WTe_2, Ag/1T′-$MoTe_2$, and $Ag_{5\%}$/1T′-$MoTe_2$, the scattering path (~ 2.80 Å) is noticeably shorter than that of Ag foil (2.89 Å) and Ag_2Te powders (2.84–2.91 Å).

Fig. 6 | DFT calculations for noble metal–TMD systems. **a**,**b**, Structures corresponding to multiple Au and Ag atoms adsorbed on 1T′-$MoTe_2$ monolayers with a noble metal/TMD ratio of 1:4 (**a**) and 3:2 (**b**). **c**, Energy diagram comparing the reduction potentials for bulk (solid lines) and atomic (dotted lines) Au and Ag adsorbed on 1T′-$MoTe_2$, as well as the Fermi level of monolayer 1T′-$MoTe_2$. Solvation effects lower the effective reduction potential of the Ag atoms from –3.91 eV to –4.03 eV, while they are almost negligible for Au atoms. **d**, Single-atom adsorption of Au and Ag on 1T′-$MoTe_2$ monolayers (noble metal:TMD = 1:12) with charge transfer analyses. Real-space charge differences ($\Delta\rho$) were integrated along *z* from the center of the vacuum area to the first zero-crossing point of $\Delta\rho$.

TOC Summary

Functionalizing two-dimensional transition metal dichalcogenide (TMD) nanosheets with noble metals is crucial for practical applications, including in catalysis and sensing, yet these processes have remained difficult to control. Now, studies on the deposition of gold and silver on a range of colloidal TMD nanostructures have shown that the noble metal–TMD interface directs the growth of either metal nanoparticles or layers.

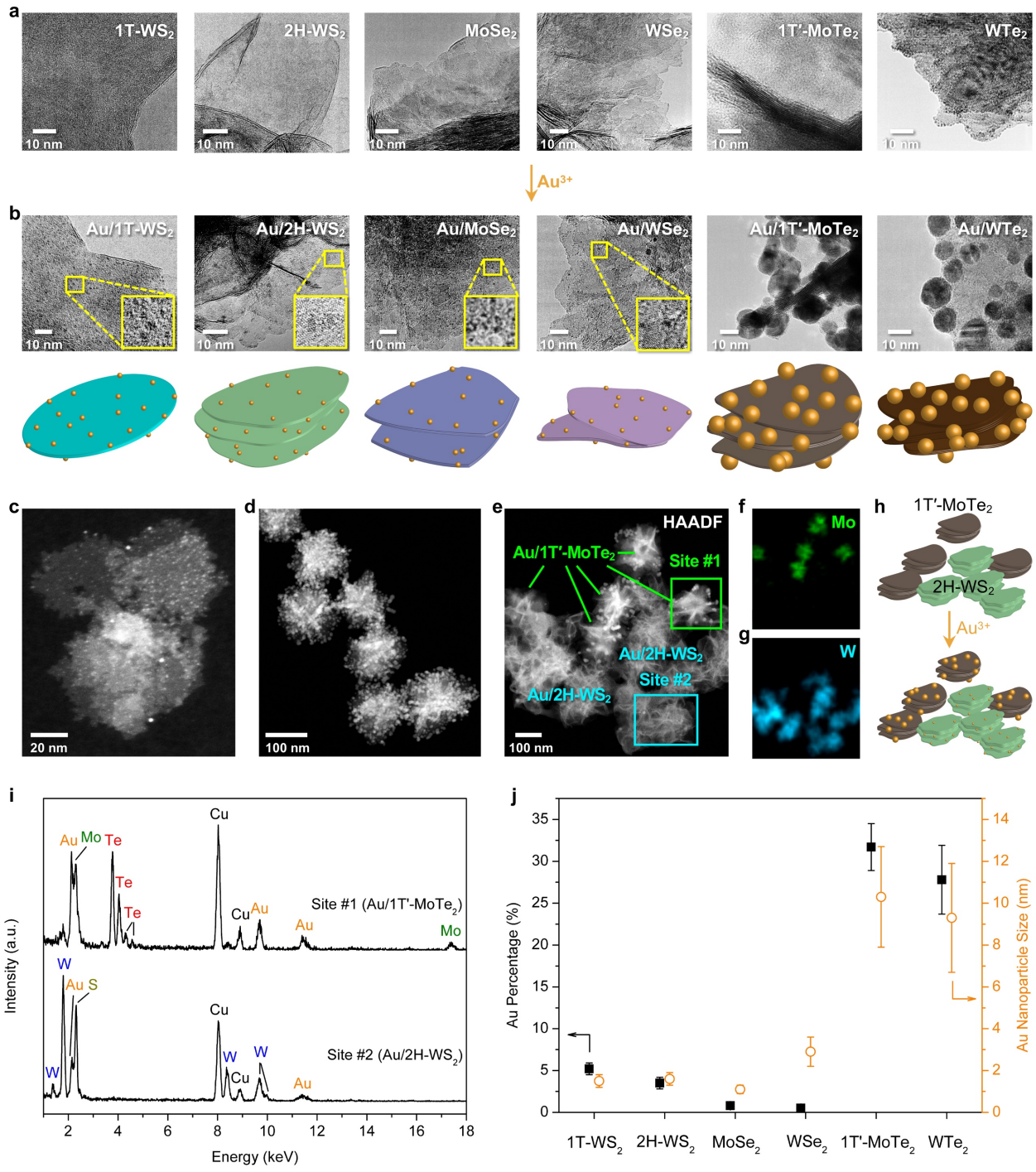
a
1T-WS2
2H-WS2
MoSe2
WSe2
1T'-MoTe2
WTe2
10 nm
Au3+
b
Au/1T-WS2
Au/2H-WS2
Au/MoSe2
Au/WSe2
Au/1T'-MoTe2
Au/WTe2
c
20 nm
d
100 nm
e
HAADF
Au/1T'-MoTe2
Site #1
Au/2H-WS2
Site #2
Au/2H-WS2
100 nm
f
Mo
g
W
h
1T'-MoTe2
2H-WS2
Au3+
i
Intensity (a.u.)
Au Mo Te
Te
Te
Cu
Cu Au
Au
Mo
Site #1 (Au/1T'-MoTe2)
W
Au S
Cu
W
W
W
Cu
Au
Site #2 (Au/2H-WS2)
Energy (keV)
j
Au Percentage (%)
Au Nanoparticle Size (nm)
1T-WS2
2H-WS2
MoSe2
WSe2
1T'-MoTe2
WTe2

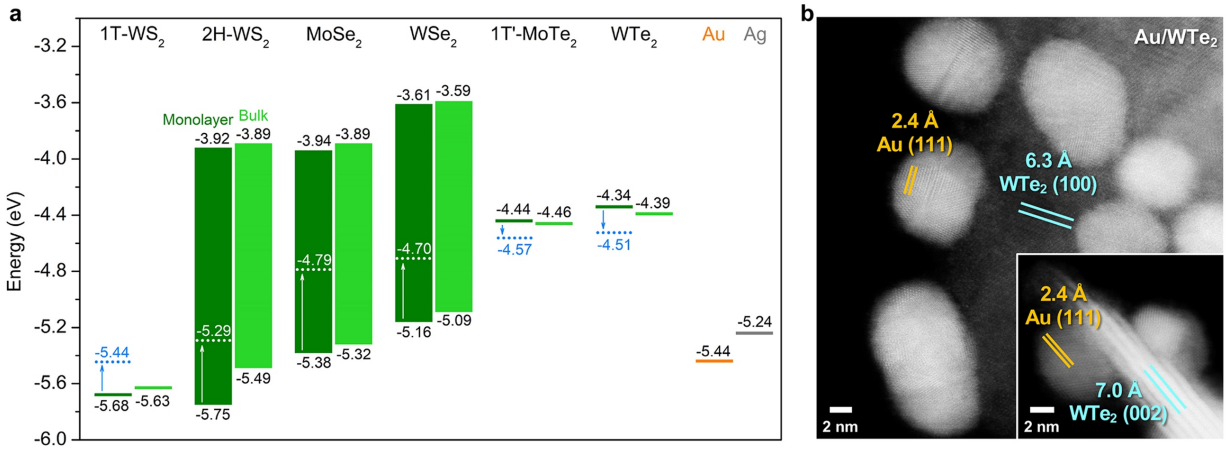
a
1T-WS2
2H-WS2
MoSe2
WSe2
1T'-MoTe2
WTe2
Au
Ag
Monolayer
Bulk
Energy (eV)
-3.2
-3.6
-4.0
-4.4
-4.8
-5.2
-5.6
-6.0
-5.44
-5.68
-5.63
-3.92
-5.29
-5.75
-3.89
-5.49
-3.94
-4.79
-5.38
-3.89
-5.32
-3.61
-4.70
-5.16
-3.59
-5.09
-4.44
-4.57
-4.46
-4.34
-4.51
-4.39
-5.44
-5.24
b
Au/WTe2
2.4 Å
Au (111)
6.3 Å
WTe2 (100)
2 nm
2.4 Å
Au (111)
7.0 Å
WTe2 (002)
2 nm

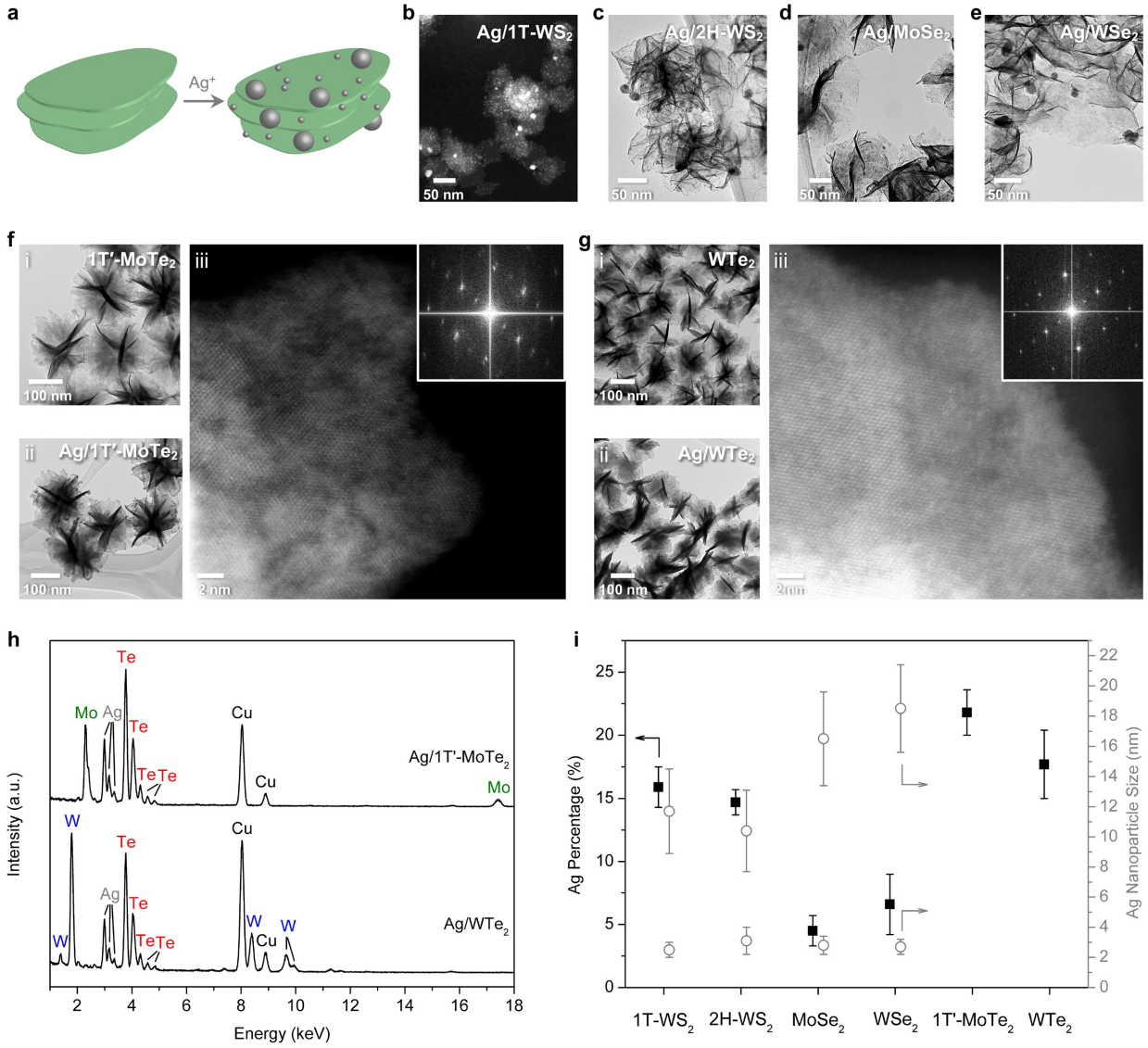
a
Ag+
b
Ag/1T-WS2
50 nm
c
Ag/2H-WS2
50 nm
d
Ag/MoSe2
50 nm
e
Ag/WSe2
50 nm
f
i
1T'-MoTe2
100 nm
ii
Ag/1T'-MoTe2
100 nm
iii
2 nm
g
i
WTe2
100 nm
ii
Ag/WTe2
100 nm
iii
2 nm
h
Intensity (a.u.)
Energy (keV)
Mo
Ag
Te
Cu
W
Ag/1T'-MoTe2
Ag/WTe2
i
Ag Percentage (%)
Ag Nanoparticle Size (nm)
1T-WS2
2H-WS2
MoSe2
WSe2
1T'-MoTe2
WTe2

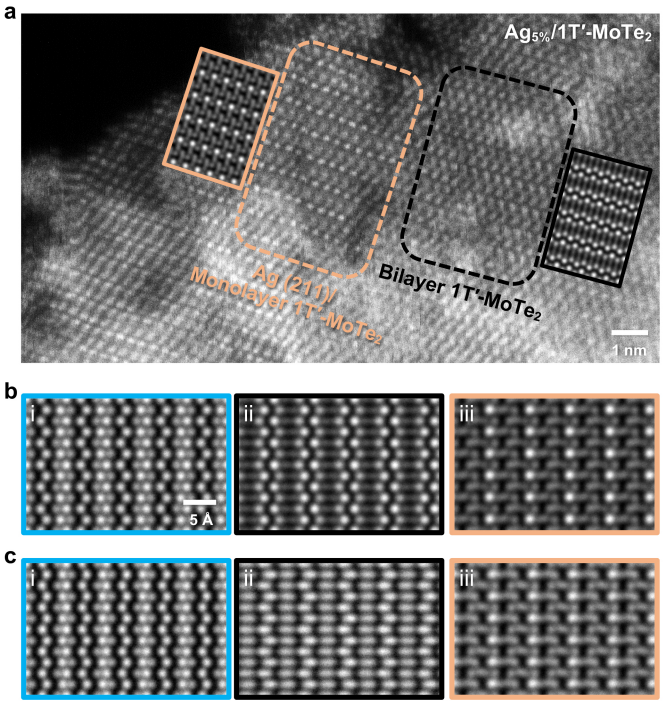
a
Ag5%/1T′-MoTe2
Ag (211)/
Monolayer 1T′-MoTe2
Bilayer 1T′-MoTe2
1 nm
b
i
ii
iii
5 Å
c
i
ii
iii

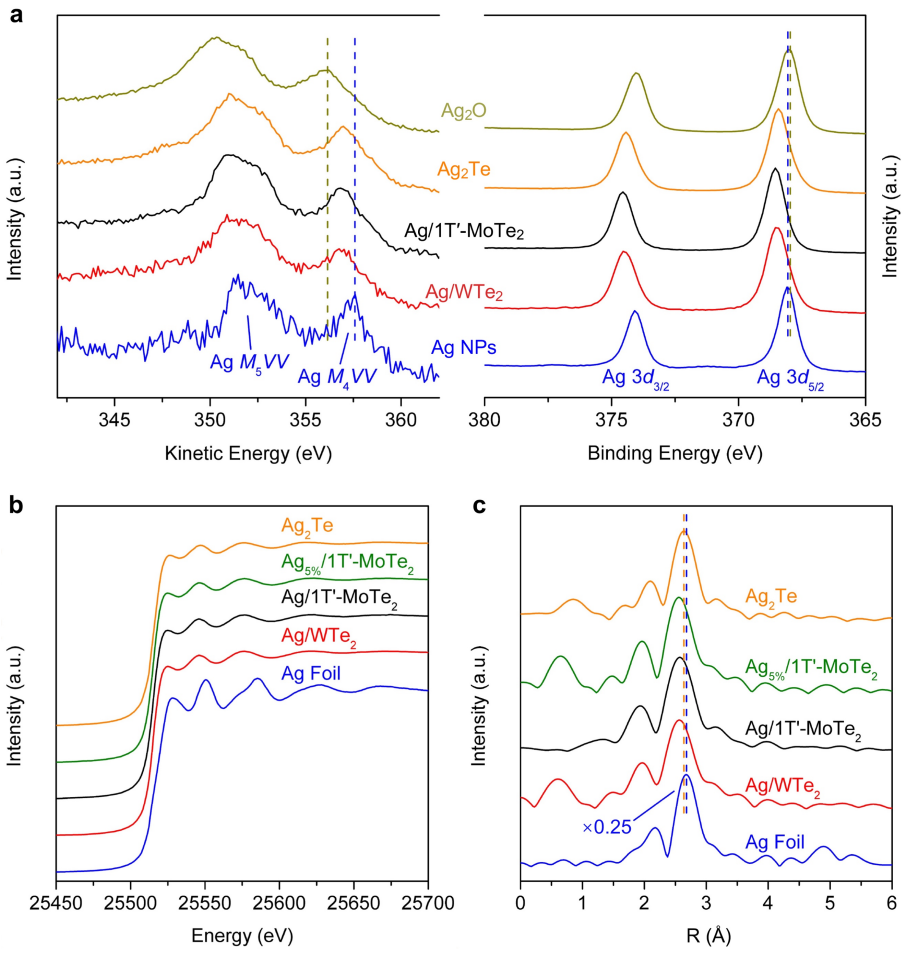
a
Intensity (a.u.)
Ag2O
Ag2Te
Ag/1T'-MoTe2
Ag/WTe2
Ag NPs
Ag M5VV
Ag M4VV
345
350
355
360
Kinetic Energy (eV)
380
375
370
365
Binding Energy (eV)
Ag 3d3/2
Ag 3d5/2
Intensity (a.u.)
b
Intensity (a.u.)
Ag2Te
Ag5%/1T'-MoTe2
Ag/1T'-MoTe2
Ag/WTe2
Ag Foil
25450
25500
25550
25600
25650
25700
Energy (eV)
c
Intensity (a.u.)
Ag2Te
Ag5%/1T'-MoTe2
Ag/1T'-MoTe2
Ag/WTe2
×0.25
Ag Foil
0
1
2
3
4
5
6
R (Å)

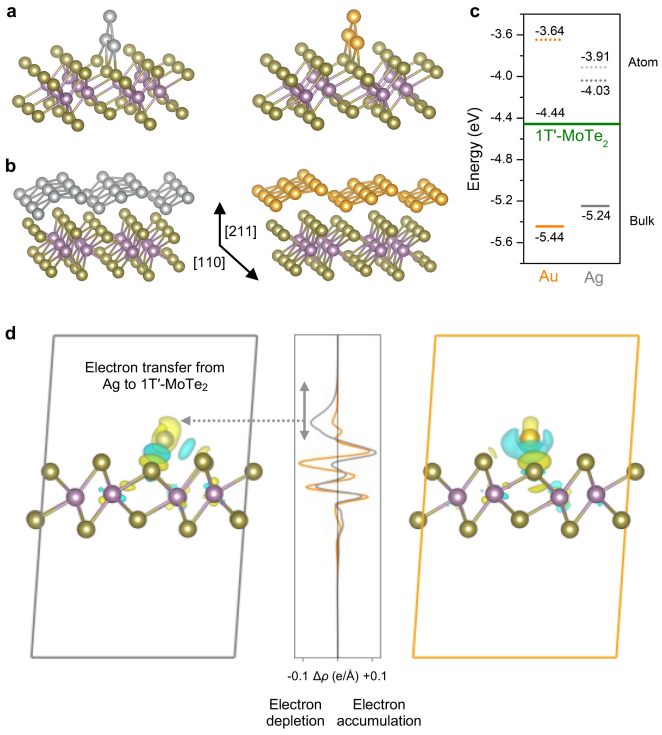
a
b
[211]
[110]
c
-3.6
-4.0
-4.4
-4.8
-5.2
-5.6
Energy (eV)
-3.64
-3.91
-4.03
Atom
-4.44
1T'-MoTe2
-5.24
Bulk
-5.44
Au
Ag
d
Electron transfer from
Ag to 1T'-MoTe2
-0.1 Δρ (e/Å) +0.1
Electron
depletion
Electron
accumulation